Superconducting isolators based on time-modulated coupled-resonator systems

Yi Zhuang,[1] Chandrashekhar Gaikwad,[2] Daria Kowsari,[2,3,4] Kater Murch,[2] and Aravind Nagulu[1,*]

[1] *Department of Electrical and Systems Engineering, Washington University, St. Louis, Missouri 63130, USA*
[2] *Department of Physics, Washington University, St. Louis, Missouri 63130, USA*
[3] *Department of Physics & Astronomy, Dornsife College of Letters, Arts, & Sciences, University of Southern California, Los Angeles, California 90089, USA*
[4] *Center for Quantum Information Science & Technology, University of Southern California, Los Angeles, California 90089, USA*

(Received 3 April 2023; revised 21 March 2024; accepted 2 May 2024; published 30 May 2024; corrected 21 August 2024)

We present a unified approach for designing isolators based on temporally modulated coupled resonator networks. Our method leverages standard superconducting quantum interference device–based resonators as building blocks, arranged in series-coupled resonators to realize a wide range of on-chip nonreciprocal devices. The devices operate by translating microwave power into out-of-band intermodulation products in a direction-dependent way. Our theoretical studies demonstrate the effectiveness of the proposed approach, achieving isolators with near-zero insertion losses and isolation greater than 20 dB. To validate our findings, we implemented and measured a series-coupled three-resonator superconducting isolator using a single-layer superconducting process. At a base temperature of 20 mK, our device exhibited an insertion loss of 1.3 dB in the forward direction and isolation of up to 25 dB at the center frequency and greater than 15 dB across a bandwidth of 250 MHz in the reverse direction. Our approach promises to enable the design of a broad range of high-performance nonreciprocal devices for superconducting circuits.

DOI: 10.1103/PhysRevApplied.21.054061

I. INTRODUCTION

Superconducting quantum systems are rapidly becoming a promising platform for building quantum computers and other quantum information-processing devices [1–3]. These systems consist of carefully engineered superconducting quantum bits (qubits) made using Josephson junctions (JJs) or a parallel combination of JJs known as superconducting quantum interference devices (SQUIDs) and are operated at millikelvin temperatures (10–100 mK) to harness quantum effects [4,5]. Nonreciprocal components, such as circulators and isolators operating at these low temperatures, are widely used to protect the qubits from the noise and spurs of the downstream electronics at higher temperatures, and to separate the input and amplified signals in quantum-limited reflection-type amplifiers [6,7]. A typical qubit-readout chain consists of three–four circulators per qubit. Currently, commercial ferrite circulators that violate Lorentz reciprocity when biased with a strong magnetic field are used for this purpose. These ferrite devices, however, cannot be integrated on chip alongside the superconducting qubits due to the significant stray flux generated by their strong magnetic bias. As a result, they are implemented as connectorized microwave components with magnetic shielding, resulting in bulky form factors and expensive implementation costs. This poses challenges for their use in large-scale quantum computing systems with thousands of qubits in a single dilution refrigerator.

Alternatively, Lorentz reciprocity can be broken using time-varying structures [6–8] and has been explored extensively in various branches of physics ranging from acoustics [9–11], electronics [7,12–17], mechanics, and optics [18–20] for realizing magnet-free, on-chip nonreciprocal devices. Recognizing the need for miniaturized and monolithically integrated nonreciprocal devices in superconducting quantum systems, prior works have explored achieving on-chip nonreciprocal devices in superconducting platforms [21–30]. Several works [21,26–29] proposed nonreciprocal circulators based on simulations, with synthetic rotation-based circulators were demonstrated in Ref. [22]. Reference [23] describes a frequency translational circulator that requires three rf pumps at separate frequencies. Traveling-wave-based nonreciprocal devices were proposed in Ref. [25] with the requirement of hundreds of Josephson junctions and a large implementation area to achieve adequate isolation. A nonmagnetic circulator with dc-flux bias was proposed in Ref. [26] and shows promise in reducing the rf pump complexity. While progress in this research area has been substantial, devices

*Corresponding author: nagulu@wustl.edu

free of high insertion loss, complex pump configurations, and near-band spurious sidebands are still lacking.

In this work, we introduce a methodology to realize a superconducting nonreciprocal isolator using the concept of temporally modulated coupled resonator networks. The concept of temporal modulation in coupled resonators was introduced to realize on-chip circulators for wireless systems [13,31]. Later, this concept was translated to realize isolating bandpass filters at rf where varactors were used as the modulating element [32,33]. Here the temporal modulation creates intermodulation (IM) products that are frequency translated away from the band of interest. By applying the modulation across a network of resonators with varying phases, the frequency translation is direction-dependent, resulting in low insertion loss in one direction and high same-frequency isolation in the reverse direction. In this work, we present a methodology to translate this concept to superconducting circuits through inductance modulation by using SQUIDs as the modulating elements. Our study showed that it is possible to utilize standard SQUID-based resonators as fundamental components that can be arranged in series-coupled resonators. This configuration allows for the implementation of on-chip nonreciprocal responses. We validate our method through the physical implementation and measurement of a series-coupled three-resonator superconducting isolator achieving >20 dB of nonreciprocity in its amplitude response. Because the nonreciprocity relies on frequency shifting of the incident tone to IM frequencies, the devices require additional elements such as diplexers to remove the out-of-band signals. To validate this potential integration, we provided simulations of the time-modulated isolators integrated with a fifth-order coupled line diplexer achieving >20-dB isolation and >50-dB IM tone suppression at the input and output ports.

The rest of the paper is structured as follows: Sec. II introduces the concept of time modulation and outlines the operation of the elementary unit cell—a time-modulated SQUID-based resonator—which serves as the fundamental building block for our nonreciprocal devices. In Sec. III, we delve into the concept, analytical studies, and simulation results of integrated nonreciprocal isolators that rely on coupled time-modulated resonators. Section IV presents the implementation and measurement results of a superconducting isolator constructed using three series-coupled SQUID-based resonators. Section V discusses the limitations and possible extensions of the proposed concept. Lastly, in Sec. VI, we conclude the paper by providing some final remarks.

II. TIME-MODULATED RESONATORS

Consider a linear time-varying (LTV) system with a modulated shunt component at a frequency ω_m. The *ABCD* network properties of a parametrically modulated shunt element can be represented as

$$\begin{bmatrix} V_1(t) \\ I_1(t) \end{bmatrix} = \begin{bmatrix} 1 & 0 \\ Y(t) & 1 \end{bmatrix} \times \begin{bmatrix} V_2(t) \\ I_2(t) \end{bmatrix}, \tag{1}$$

where $V_{1,2}(t)$ and $I_{1,2}(t)$ are the voltages and currents at ports 1 and 2, respectively. By taking a Fourier transform of the system in Eq. (1), one can show that the port voltages and currents carry the intermodulation signal between the input and the pump frequencies, namely, they contain the frequency component at $(\omega_{in} \pm k\omega_m)$ where $k = 0, \pm 1, \pm 2, \ldots$ In the spectral domain, such a time-modulated system can be represented as

$$\begin{bmatrix} \underline{V_1} \\ \underline{I_1} \end{bmatrix} = \begin{bmatrix} \underline{U} & \underline{0} \\ \underline{Y} & \underline{U} \end{bmatrix} \times \begin{bmatrix} \underline{V_2} \\ \underline{I_2} \end{bmatrix}, \tag{2}$$

where $\underline{V_{1,2}}$ and $\underline{I_{1,2}}$ are column vectors of size $(2N+1)$ with Fourier coefficients of frequency components $(\omega_{in} \pm k\omega_m)$, $k = [-N, -(N-1), \ldots, 0, \ldots, N-1, N]$, $\underline{Y}$ represents the spectral admittance matrix of the shunt element (see Sec. A for more details), $\underline{U}$ and $\underline{0}$ are the identity and zero matrices [34,35]. The value of N determines the accuracy of the spectral domain computation.

A. Spectral admittance matrix of a dc SQUID

JJs are superconducting devices made by sandwiching a thin layer of insulator between two superconducting layers [4,5]. A SQUID consists of two JJs in parallel and its inductance is controlled by modulating the magnetic flux threading the junction loop. The inductance of a SQUID can be expressed as

$$L_{SQUID} = \frac{\Phi_0}{4\pi I_c |\cos(\pi\Phi/\Phi_0)|}, \tag{3}$$

where I_c is the critical current of the JJs, Φ is the magnetic flux threading the SQUID loop, and Φ_0 is the flux quantum. It has to be noted that Eq. (3) is applicable for signal currents that are smaller than the critical current. Hence the power handling of the SQUID is limited by the value of critical current. The power handling of the SQUID can be increased by using an array of concatenated SQUID loops and the inductance of an N-stacked SQUID array multiplied by a factor of N. From Eq. (3), the inductance of a flux-modulated SQUID with sinusoidal modulation can be expressed as

$$\frac{1}{L(t)} = \frac{4\pi I_c}{\Phi_0} \cos\left(\frac{\pi(\Phi_{DC} + \Delta\Phi\cos(\omega_m t + \theta))}{\Phi_0}\right). \tag{4}$$

Here the sinusoidal modulation is assumed to be small to satisfy the relation $(\Delta\Phi + \Phi_{DC}) < \Phi_0/2$, thus resulting in a positive inductance value. The cosine term can be expanded and simplified using Taylor expansions as

$$\cos\left(\pi\frac{\Delta\phi\cos(\omega_{\rm m}t+\theta)}{\phi_0}\right)\approx\left[1-\frac{1}{4}\left(\frac{\pi\Delta\phi}{\phi_0}\right)^2\right]+\cos(2\omega_{\rm m}t+2\theta)\left[-\frac{1}{4}\left(\frac{\pi\Delta\phi}{\phi_0}\right)^2\right], \tag{5}$$

$$\sin\left(\pi\frac{\Delta\phi\cos(\omega_{\rm m}t+\theta)}{\phi_0}\right)\approx\sin(\omega_{\rm m}t+\theta)\left[\left(\frac{\pi\Delta\phi}{\phi_0}\right)-\frac{1}{8}\left(\frac{\pi\Delta\phi}{\phi_0}\right)^3\right]+\sin(3\omega_{\rm m}t+3\theta)\left[\frac{1}{24}\left(\frac{\pi\Delta\phi}{\phi_0}\right)^3\right]. \tag{6}$$

Further, the inductance of the SQUID can be approximated as

$$\frac{1}{L(t)}\approx\sum_{p=-3}^{3}F_p e^{jp\times\theta}e^{jp\omega_{\rm m}t}, \tag{7}$$

where the constants are

$$F_0=\frac{4\pi I_{\rm c}}{\Phi_0}\cos\left(\frac{\pi\Phi_{\rm DC}}{\Phi_0}\right)\left[1-\frac{1}{4}\left(\frac{\pi\Delta\Phi}{\Phi_0}\right)^2\right], \tag{8}$$

$$F_{-1}=-F_1=\frac{2\pi I_{\rm c}}{j\,\Phi_0}\sin\left(\frac{\pi\Phi_{\rm DC}}{\Phi_0}\right)\left[\left(\frac{\pi\Delta\Phi}{\Phi_0}\right)-\frac{1}{8}\left(\frac{\pi\Delta\Phi}{\Phi_0}\right)^3\right], \tag{9}$$

$$F_{-2}=F_2=\frac{2\pi I_{\rm c}}{\phi_0}\cos\left(\frac{\pi\phi_{\rm DC}}{\phi_0}\right)\left[-\frac{1}{4}\left(\frac{\pi\Delta\phi}{\phi_0}\right)^2\right], \tag{10}$$

$$F_{-3}=-F_3=\frac{2\pi I_{\rm c}}{\phi_0}\sin\left(\frac{\pi\phi_{\rm DC}}{\phi_0}\right)\left[\frac{1}{24}\left(\frac{\pi\Delta\phi}{\phi_0}\right)^3\right]. \tag{11}$$

The spectral representation of time-varying inductance is discussed in Appendix A. Finally, from Eq. (7), the spectral admittance of a flux-modulated SQUID can be expressed as

$$\underline{Y_L}=\begin{bmatrix}
\ddots & \vdots & \vdots & \vdots & \vdots & \vdots & \iddots\\
\cdots & \frac{F_0}{j(\omega-2\omega_{\rm m})} & \frac{F_{-1}e^{-j\theta}}{j(\omega-\omega_{\rm m})} & \frac{F_{-2}e^{-j2\theta}}{j\omega} & \frac{F_{-3}e^{-j3\theta}}{j(\omega+\omega_{\rm m})} & 0 & \cdots\\
\cdots & \frac{F_1e^{j\theta}}{j(\omega-2\omega_{\rm m})} & \frac{F_0}{j(\omega-\omega_{\rm m})} & \frac{F_{-1}e^{-j\theta}}{j\omega} & \frac{F_{-2}e^{-j2\theta}}{j(\omega+\omega_{\rm m})} & \frac{F_{-3}e^{-j3\theta}}{j(\omega+2\omega_{\rm m})} & \cdots\\
\cdots & \frac{F_2e^{j2\theta}}{j(\omega-2\omega_{\rm m})} & \frac{F_1e^{j\theta}}{j(\omega-\omega_{\rm m})} & \frac{F_0}{j\omega} & \frac{F_{-1}e^{-j\theta}}{j(\omega+\omega_{\rm m})} & \frac{F_{-2}e^{-j2\theta}}{j(\omega+2\omega_{\rm m})} & \cdots\\
\cdots & \frac{F_3e^{j3\theta}}{j(\omega-2\omega_{\rm m})} & \frac{F_2e^{j2\theta}}{j(\omega-\omega_{\rm m})} & \frac{F_1e^{j\theta}}{j\omega} & \frac{F_0}{j(\omega+\omega_{\rm m})} & \frac{F_{-1}e^{-j\theta}}{j(\omega+2\omega_{\rm m})} & \cdots\\
\cdots & 0 & \frac{F_{-3}e^{-j3\theta}}{j(\omega-\omega_{\rm m})} & \frac{F_{-2}e^{-j2\theta}}{j\omega} & \frac{F_{-1}e^{-j\theta}}{j(\omega+\omega_{\rm m})} & \frac{F_0}{j(\omega+2\omega_{\rm m})} & \cdots\\
\iddots & \vdots & \vdots & \vdots & \vdots & \vdots & \ddots
\end{bmatrix}. \tag{12}$$

It is worthwhile to note that, the up-conversion and down-conversion frequency translational terms of a single time-modulated SQUID have reciprocal magnitude response and nonreciprocal phase response.

B. Unit cell: a time-modulated SQUID-based resonator

The building block of the time-modulated nonreciprocal components developed in this paper is a resonator consisting of a flux-modulated SQUID in parallel with a capacitor as shown in Fig. 1(a). The *ABCD* matrix of the unit cell can be written as

$$\begin{bmatrix}\underline{V_1}\\ \underline{I_1}\end{bmatrix}=\begin{bmatrix}\underline{U} & \underline{0}\\ \underline{Y_{LC}} & \underline{U}\end{bmatrix}\times\begin{bmatrix}\underline{V_2}\\ \underline{I_2}\end{bmatrix}, \tag{13}$$

where $\underline{Y_{LC}}=\underline{Y_L}+\underline{Y_C}$, $\underline{Y_L}$ and $\underline{Y_C}$ is the spectral admittance matrix of the flux-modulated SQUID and capacitor. Since

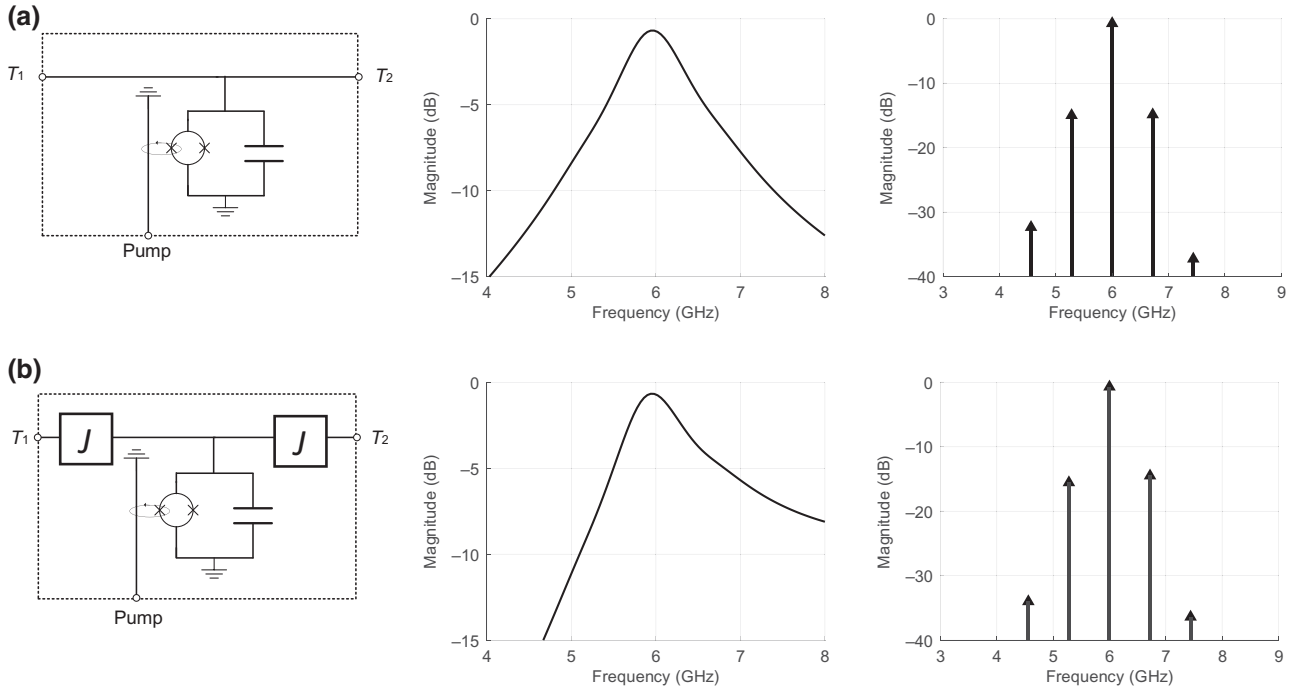

FIG. 1. Schematic, transmission response, and normalized output spectra of a time modulated (a) unit cell realized using SQUID and a capacitor, and (b) unit cell sandwiched between two J inverters. The IM products can be seen as sidebands on the carrier at 6 GHz. In both cases, the SQUID is biased at $\Phi_{DC} = 0.35\Phi_0$, and modulated with $\Delta\Phi = 0.025\Phi_0, f_m = 0.7$ GHz, and an input signal is incident on port 1 at the center frequency, $f_{in} = f_{center} = 6$ GHz.

the capacitor is just a static element, $\underline{Y_C}$ reduces to a diagonal matrix with each entry corresponding to the admittance of the capacitance at the corresponding intermodulation frequency. Figure 1(a) also depicts the frequency response and normalized output spectra of a time-modulated resonator with $\Delta\Phi = 0.025\Phi_0$, $f_m = 0.7$ GHz, and an input signal at the center frequency $f_{in} = f_{center} = 6$ GHz. The time-modulated resonators exhibit a reciprocal response with nonzero loss due to the frequency conversion of the input power to intermodulation frequencies. In Sec. III, we will show how multiple resonators can be coupled to create a direction-dependent frequency translation, thus realizing a nonreciprocal amplitude response.

C. Unit cell with admittance inverter

To enable coupling between resonator networks, we sandwich our unit cell between two admittance inverters (J inverters) as shown in Fig. 1(b). Since the admittance inverters are time invariant, the *ABCD* matrix is

$$M_J = \begin{bmatrix} \underline{0} & \pm\frac{1}{jJ}\underline{U} \\ \pm jJ\underline{U} & \underline{0}. \end{bmatrix}, \tag{14}$$

where $1/J$ is the characteristic impedance of the impedance inverter, and $j = \sqrt{-1}$. An appropriate value of the J-inverter admittance can be chosen to create the required coupling [36]. The spectral *ABCD* matrix of a unit cell with J inverters can be expressed as

$$\begin{aligned} \begin{bmatrix} \underline{V_1} \\ \underline{I_1} \end{bmatrix} &= [M_J \times M_{LC} \times M_J] \times \begin{bmatrix} \underline{V_2} \\ \underline{I_2} \end{bmatrix}, \\ &= \begin{bmatrix} \underline{U} & (\underline{Y_{LC}})/J^2 \\ \underline{0} & \underline{U} \end{bmatrix} \times \begin{bmatrix} \underline{V_2} \\ \underline{I_2} \end{bmatrix}. \end{aligned} \tag{15}$$

As shown in Fig. 1(b), the transmission response and the frequency-translation features of the unit cell remain similar to Fig. 1(a). However, the J inverters enable us to create coupling between two unit cells, which is essential for creating a coupled resonator network and therefore nonreciprocal devices.

III. SUPERCONDUCTING NONRECIPROCAL DEVICES BASED ON TIME-MODULATED COUPLED RESONATOR NETWORKS

In modern circuit design, the ability to achieve nonreciprocal response is essential. One approach to realize such a response is by coupling several unit cells together using J inverters, thus introducing a spatiotemporal modulation. In addition, these temporally modulated unit cells can be connected in various circuit topologies such as series coupling, wye coupling, δ coupling, and two-dimensional (2D) lattices [13,33,37,38]. Each of these topologies can

exhibit unique nonreciprocal behavior such as isolation, circulation, and topological robustness. In this section, we will discuss these circuit topologies and analyze their nonreciprocal behavior using the spectral-*ABCD* matrices. Specifically, we will investigate the factors that influence the nonreciprocal behavior, such as the modulation scheme and the arrangement of the unit cells. Understanding these dependencies allows us to design circuits with tailored nonreciprocal responses to meet specific application requirements. A similar theoretical study of time-modulated, coupled-resonator networks was reported in Ref. [39].

A. Amplitude nonreciprocity using coupled unit cells

When multiple time-varying elements are coupled, the input signal will be up-converted (down-converted) by one resonator and the generated IM products can be down-converted (up-converted) back to the input frequency by another resonator. From Sec. II, we have seen that a single time-varying resonator results in the same conversion gain for the up-conversion and down-conversion to IM products, but results in a nonreciprocal phase relation. The nonreciprocal phase relation was not emphasized in Sec. II. Therefore, if we introduce a phase staggering between the pumping signals of two time-varying resonators, the phase of the signal that gets reconstructed back to the input frequency would depend on the phase difference between the pumping signals. Under optimal modulation conditions the reconstructed input signal can add up destructively or constructively depending on the incident signal direction, thus resulting in nonreciprocal amplitude response.

This scenario can be illustrated using a simple system with two unit cells that are coupled with one J inverter and are modulated with $\Phi_{\text{pump1}} = \Delta\Phi\cos(\omega_{\text{m}}t + \theta_1)$ and $\Phi_{\text{pump2}} = \Delta\Phi\cos(\omega_{\text{m}}t + \theta_2)$. For the sake of simplicity and intuitive understanding, only the first IM conversion is considered in this illustration. However, for a more precise performance evaluation, conversions to other IM frequencies should also be taken into account, as done in the later sections. The network *ABCD* parameters of this system can be expressed as

$$\begin{aligned}\begin{bmatrix}\underline{V_1}\\ \underline{I_1}\end{bmatrix} &= [M_{LC,1}\times M_J \times M_{LC,2}]\times\begin{bmatrix}\underline{V_2}\\ \underline{I_2}\end{bmatrix},\\ &= \begin{bmatrix}\dfrac{1}{jJ}\underline{Y_{LC,2}} & \dfrac{1}{jJ}\underline{U}\\ jJ\underline{U}+\dfrac{1}{jJ}\underline{Y_{LC,1}}\cdot\underline{Y_{LC,2}} & \dfrac{1}{jJ}\underline{Y_{LC,1}}\end{bmatrix}\times\begin{bmatrix}\underline{V_2}\\ \underline{I_2}\end{bmatrix},\end{aligned} \tag{16}$$

where $M_{LC,1}$ and $M_{LC,2}$ are the spectral-*ABCD* matrices of the first and second resonators, M_J is the spectral *ABCD* matrix of the coupling J inverter, and

$$\underline{Y_{LC,1}} = \begin{bmatrix}\ddots & \vdots & \vdots & \vdots & \iddots\\ \cdots & \dfrac{F_0-(\omega-\omega_{\text{m}})^2C}{j(\omega-\omega_{\text{m}})} & \dfrac{F_{-1}e^{-j\theta_1}}{j\omega} & \dfrac{F_{-2}e^{-j2\theta_1}}{j(\omega+\omega_{\text{m}})} & \cdots\\ \cdots & \dfrac{F_1e^{j\theta_1}}{j(\omega-\omega_{\text{m}})} & \dfrac{F_0-\omega^2C}{j\omega} & \dfrac{F_{-1}e^{-j\theta_1}}{j(\omega+\omega_{\text{m}})} & \cdots\\ \cdots & \dfrac{F_2e^{j2\theta_1}}{j(\omega-\omega_{\text{m}})} & \dfrac{F_1e^{j\theta_1}}{j\omega} & \dfrac{F_0-(\omega+\omega_{\text{m}})^2C}{j(\omega+\omega_{\text{m}})} & \cdots\\ \iddots & \vdots & \vdots & \vdots & \ddots\end{bmatrix}, \tag{17}$$

where F_0, F_{-1}, and F_1 are expressed in Eqs. (8) and (9). Similarly, $\underline{Y_{LC,2}}$ can be expressed in terms of θ_2. The transmission scattering parameter of this network can be expressed as

$$\begin{aligned}\underline{S_{21}} &= 2[\underline{A}+\underline{B}/Z_0+\underline{C}Z_0+\underline{D}]^{-1}\\ &= \frac{j}{J}[\underline{Y_{LC,2}}+\underline{Y_{LC,1}}+\frac{\underline{U}}{Z_0}-J^2Z_0\underline{U}+Z_0\underline{Y_{LC,1}}.\underline{Y_{LC,2}}]^{-1},\end{aligned} \tag{18}$$

and by symmetry, one can show that

$$\underline{S_{12}} = \frac{j}{J}\left[\underline{Y_{LC,1}}+\underline{Y_{LC,2}}+\frac{\underline{U}}{Z_0}-J^2Z_0\underline{U}+Z_0\underline{Y_{LC,2}}.\underline{Y_{LC,1}}\right]^{-1}. \tag{19}$$

The eigenvalues of $\underline{Y_{LC,1}}$ and $\underline{Y_{LC,2}}$ are different when $\theta_1 \neq \theta_2$, thereby making these matrices noncommuting (i.e., $\underline{Y_{LC,2}}.\underline{Y_{LC,1}} \neq \underline{Y_{LC,1}}.\underline{Y_{LC,2}}$), resulting in nonreciprocal

scattering matrices. By choosing an appropriate modulation amplitude, modulation frequency, and phase difference, one can design for $S_{21} \approx 1$ and $S_{12} \approx 0$ for the input and output frequency of ω, thus resulting in an isolator.

B. Isolator using time-modulated series-coupled resonators

Traditional bandpass filters (such as Butterworth, Chebyshev, etc.) are typically implemented by coupling multiple LC resonators using admittance inverters. The number of resonators, their coupling, and loaded quality factor are chosen to achieve the desired filter characteristics, such as bandwidth, out-of-band rejection, and in-band ripple [36]. Following a similar architecture, we couple multiple unit cells through J inverters as shown in Fig. 2(a). Similar to a conventional LC filter, the static flux-biased SQUIDs, the parallel capacitors, and the admittance of the J inverters can be chosen to realize a specific bandpass filter response. When the SQUIDs are biased with a dc flux, the lack of frequency translation results in a reciprocal transmission through the filter.

However, modulating the SQUIDs within each resonator with sinusoidal flux pumps that have staggered phase shifts would result in a nonreciprocal transmission response in the circuit. In this scenario, the incident signal is first translated to the intermodulation frequencies ($f_{\text{in}} \pm kf_{\text{m}}$) and then reconstructed back to the input frequency. The different phase staggering in the pump signals encountered by the input signal in the forward direction leads to constructive addition of the reconstructed IM products in one direction, resulting in low insertion loss. Conversely, in the opposite direction, the reconstructed IM products add up destructively, resulting in high isolation [33]. The response of the filter can be analyzed in the same fashion as presented in Sec. III A.

The $ABCD$ matrix of the filter is a cascade of the $ABCD$ of all the admittance inverters and unit cells, that is

$$M_{\text{BPF}} = M_{J_1} M_{LC_1} M_{J_2} M_{LC_2} \cdots M_{J_{n-1}} M_{LC_{n-1}} M_{J_n}, \quad (20)$$

where M_{J_1}, M_{J_2}, $M_{J_{n-1}}$, and M_{J_n} are the spectral-$ABCD$ matrices of the admittance inverters and M_{LC_1}, M_{LC_2}, and $M_{LC_{n-1}}$ are the spectral-$ABCD$ matrices of the unit cells. Therefore, substituting Eqs. (13) and (14) into Eq. (20) results in the $ABCD$ matrix of the filter. Figure 2(b) shows the simulation responses of a second-order bandpass filter optimized for maximum nonreciprocity. However, due to limited degrees of freedom and frequency translational paths for converting the intermodulation (IM) products back to the input signal, the second-order BPF exhibits a high insertion loss of 4.64 dB when optimized for an isolation of 20 dB. Increasing the number of resonators within the bandpass filter would result in more degrees of freedom and would enable us to achieve both low insertion loss and high isolation. Therefore, higher-order filters such as third-order and fourth-order filters [shown in Figs. 2(c) and 2(d), respectively] can be used to achieve near-zero insertion loss while providing high isolation. Figures 2(e)

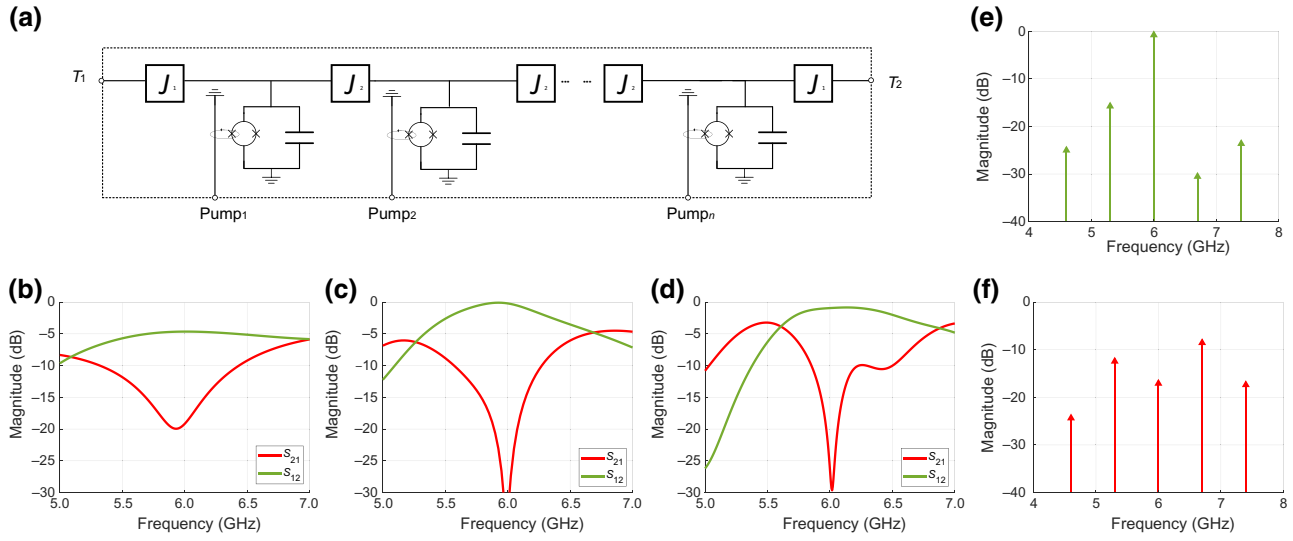

FIG. 2. (a) A general solution of building a SQUID-based higher-order bandpass filter. Response of a time-modulated nonreciprocal bandpass filter with (b) two coupled resonators, (c) three coupled resonators, and (d) four coupled resonators using modulation parameters of $\Phi_{\text{dc}} = 0.35\Phi_0$, $\Delta\Phi = 0.025\Phi_0$, $f_{\text{m}} = 700$ MHz, and $\theta = 90^\circ$. Simulated output spectra in (e) transmission and (f) isolation directions of a third-order nonreciprocal bandpass filter for an input excitation at the center frequency. The transmission and isolation asymmetry in the in-band frequency (near 6 GHz) is due to the direction-dependent scattering into the IM frequencies. Care should be taken to make sure that these IM products are removed, or the operation conditions are robust to the presence of these out-of-band components.

and 2(f) depict the normalized output spectrum of a third-order filter in the transmission and the isolation directions, respectively. Consistent with the scattering parameters, the filter achieves low insertion loss in the forward direction and high isolation in the reverse direction.

IV. IMPLEMENTATION AND MEASUREMENTS OF A THREE-RESONATOR-COUPLED ISOLATOR

In this paper, we focused on a detailed analysis of a third-order bandpass filter as it offers low insertion loss, high isolation, and requires less chip area. To maintain consistency with the design implemented in Sec. IV, we carried out the analytical analysis on a third-order bandpass filter designed to operate at 6 GHz with a bandwidth of 700 MHz. This coupled-resonator isolator consists of four modulation parameters, namely (i) static flux bias Φ_{dc}, (ii) modulation amplitude $\Delta\Phi$, (iii) modulation frequency f_m, and (iv) modulation phase staggering θ. Figure 3 depicts the theoretical study of the forward and reverse transmission responses across varying modulation parameters, which was performed using the spectral-*ABCD* matrices. Figure 3(a) shows the tunability in the center frequency of the isolator across varying static flux bias. Low insertion loss <0.5 dB and high isolation >20 dB can be achieved across a tuning bandwidth of 1.9 GHz by tuning the static flux bias from $0.3\Phi_0$ to $0.4\Phi_0$. Figure 3(b) depicts the performance across modulation flux amplitude. As expected, when the amplitude decreases to 0, the filter approaches the static design. We found that a flux modulation amplitude of $0.024\Phi_0$ results in the optimal insertion loss while achieving a high isolation. Figure 3(c) suggests that when the modulation frequency approaches the bandwidth of the static BPF, it results in the best isolation. Finally, Fig. 3(d) shows that the filter can achieve nonreciprocity with phase staggering ranging from 40° to 120°. Within this range, higher phase staggering results in higher isolation, however with a reduced transmission bandwidth. We choose to operate with a phase staggering of 90° as it achieves a low insertion loss of 0.4 dB and a high isolation of 25 dB. Additionally, note that the transmission and the isolation are off symmetric with respect to each other when $\theta = \theta + 180°$. Therefore, the transmission and the isolation directions of the isolator can be easily tuned by changing the phase staggering to 270°. Overall, the coupled-resonator-based isolator could result in low insertion loss, high isolation, and tunability in the center frequency and direction of transmission within a compact area on a superconducting chip.

Figure 4 depicts the schematic of the implemented isolator using three coupled resonators. To achieve a compact chip area, the admittance inverters used for the coupling are realized using π-capacitive structure. The negative shunt capacitors required within the π capacitive are realized by appropriately reducing the shunt-capacitor value within the SQUID resonators.

A. Design procedure

First, a conventional bandpass filter is designed to operate at 6 GHz with a 1-dB bandwidth of 700 MHz

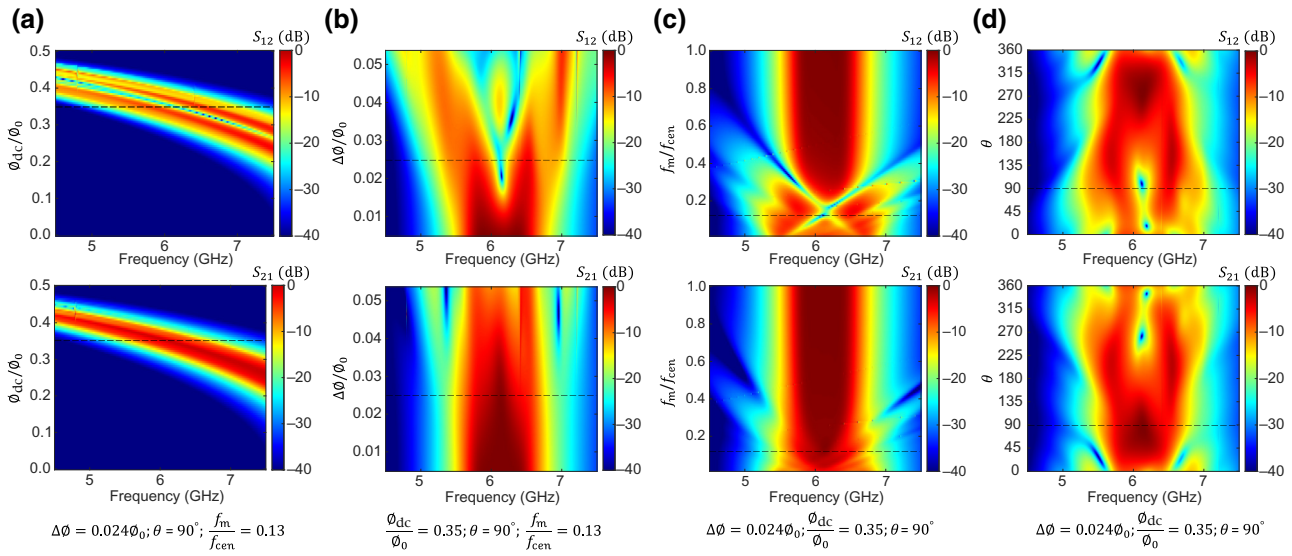

FIG. 3. Theoretical studies of the time-modulated isolator with three coupled resonators. Modulated $S_{12(0,0)}$ and $S_{21(0,0)}$ with varying (a) static flux bias Φ_{DC}, (b) modulation amplitude $\Delta\phi$, (c) modulation frequency f_m, and (d) phase staggering θ. Here $S_{21(0,0)}(S_{12(0,0)})$ represents the transmission from port 1 (port 2) to port 2 (port 1) for the same input and output frequencies. The dashed lines represent the optimal biasing for transmission from port 1 to port 2 and isolation from port 2 to port 1. The solid line in panel (d) represents the optimal phase biasing for transmission in the reverse direction.

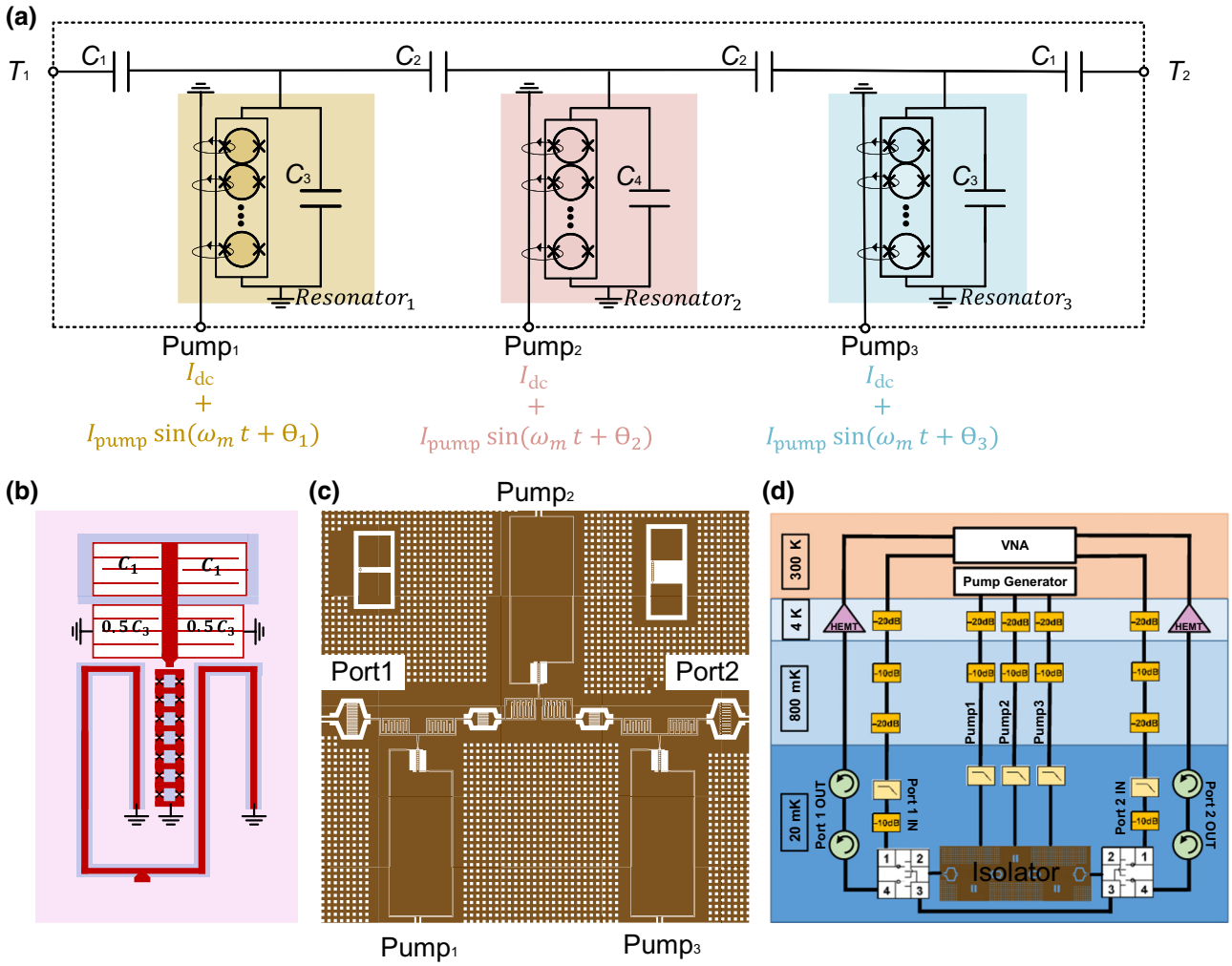

FIG. 4. The schematic of the implemented isolator with three coupled resonators and stacked SQUIDs. (b) The layout of the unit cell with capacitive admittance inverters. (c) Chip microphotograph. (d) Measurement block diagram of the experimental setup.

and matching of <-15 dB, and high out-of-band rejection using ten-stacked SQUIDs each with $I_c = 4$ μA, $\Phi_{dc} = 0.35\Phi_0$, and the capacitors $C_1 = 257$ fF, $C_2 = 113$ fF, $C_3 = 232$ fF, and $C_4 = 284$ fF. Then a sinusoidal modulation with progressive phase shifts is imparted to the feed currents to achieve nonreciprocal response, i.e., $\Phi_{feed,i} = \Phi_{dc} + \Delta\Phi\cos(\omega_m t + (i-1)\times\theta)$ where i represents the resonator number from left to right. The filter performance is optimized across the parameter space of $\Delta\Phi, \omega_m, \theta$, and Φ_{dc} for low insertion loss in the forward direction and high isolation in the reverse direction using the parametric study based on spectral-*ABCD* matrices in Fig. 3. For an optimal modulation condition of $\Phi_{dc} = 0.35\Phi_0$, $\Delta\Phi = 0.024\Phi_0$, $f_m = 700$ MHz, and $\theta = 90°$, at a center frequency of 6 GHz, the post-layout EM simulated filter exhibits an insertion loss of 0.6 dB in the forward direction and isolation >25 dB in the reverse direction. Additionally, the center frequency of the nonreciprocal bandpass filter can be tuned by varying the dc flux bias of the SQUID loops from 5.2 to 7.1 GHz while achieving sub-1-dB insertion loss and >20-dB isolation. A similar architecture achieving the isolator functionality has also been explored in Ref. [30], however, it uses a suboptimal phase difference of $\theta = 45°$ between the resonators, which results in higher fundamental insertion loss as shown in Fig. 3(d).

B. Implementation and fabrication

The isolator is fabricated using an in-house single-layer aluminum process. The JJs in the filter are realized using the Dolan bridge technique and an electron-beam lithography process on a bilayer resist stack with an insulator thickness of 2 to 5 nm. The required JJ critical current 4 μA is realized using 4×0.5 μm^2 junctions with a critical current density of 2 μA/μm^2. The SQUID loops in the filter have a conductor width of 4 μm and occupy a total area of 16×16.5 μm^2 with a loop area of 8×8.5 μm^2. The

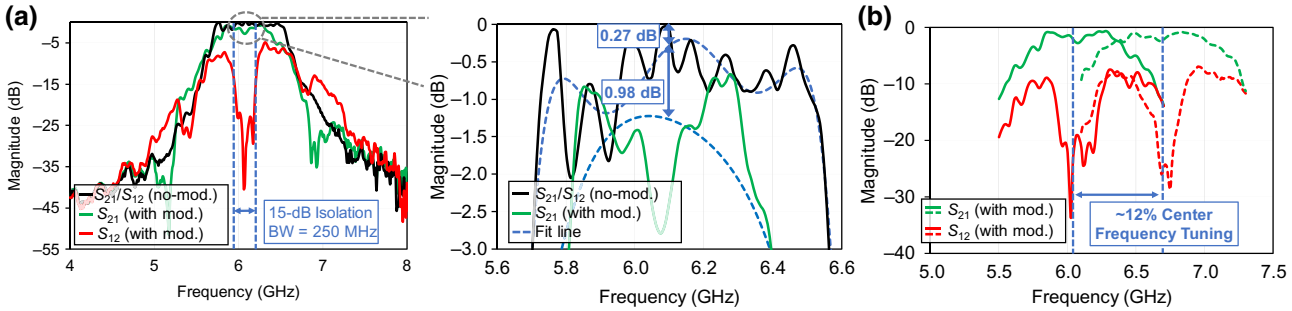

FIG. 5. Measured small signal performance of the coupled-resonator-based isolator: (a) transmission when no modulation is applied (black curve), transmission (green curve), and isolation (red curve) when optimal pump modulation is applied. (b) Measured center frequency tuning by leveraging the dc flux bias of the SQUIDs in the resonators.

EM simulated geometric loop inductance of the SQUIDs is 12 pH, which is approximately 20% of the SQUID inductance at zero flux bias. The capacitors in the design are created with a conventional fingered-capacitor layout with self-resonance frequency >10 GHz. To reduce the capacitive coupling between the feed-line and SQUID loops, a pseudodifferential coupling strategy is employed for the pump line as shown in Fig. 4(b). The nonreciprocal bandpass filter occupies an area of 3 mm^2 and the input-output and pump signals are connected to the chip edge using coplanar waveguide launchers.

C. Measurement results

The layout of the fabricated nonreciprocal bandpass filter is shown in Fig. 4(c). The device is wire bonded to a PCB and is mounted in a copper package. The input-output terminals of the bandpass filter and three pump lines are linked to five of the eight rf lines within the copper package. The package is placed inside a dilution refrigerator with a base temperature of 20 mK and surrounded by cryoperm shielding to provide additional protection again external magnetic fields. Figure 4(d) outlines the setup used for the measurement. The input-output terminals of the isolator are connected to the probe and readout lines in the dilution refrigerator through two SMA latch transfer switches (model no. Radiall R577432000). A through line is also connected between the remaining ports of the switches in order to measure the transmission loss and/or gain of the probe and readout lines inside the dilution refrigerator.

Figure 5(a) depicts the measured scattering parameters of the nonreciprocal bandpass filter after normalizing with the transmission loss of the through structure. The measured transmission loss of the filter with no modulation is 0.27 dB (black curve), which could be due to the imperfections in the gain-based calibration. When flux pumping is applied to achieve nonreciprocity, we measured an additional insertion loss of 0.98 dB in the forward direction (green curve). The measured isolation is +25 dB at the center frequency and is >15 dB across 250-MHz bandwidth in the reverse direction. Additionally, the dc flux bias can be leveraged to tune the center frequency of the bandpass filter from 6 to 6.75 GHz as shown in Fig. 5(b). A small ripple in the transmission response is due to the mismatches within the probe and readout lines. This can be avoided by employing a full two-port characterization [40]. Figure 6(a) depicts the transmission loss of the filter across varying input powers. We measured the −1-dB compression point to be −68 dBm, which is several orders

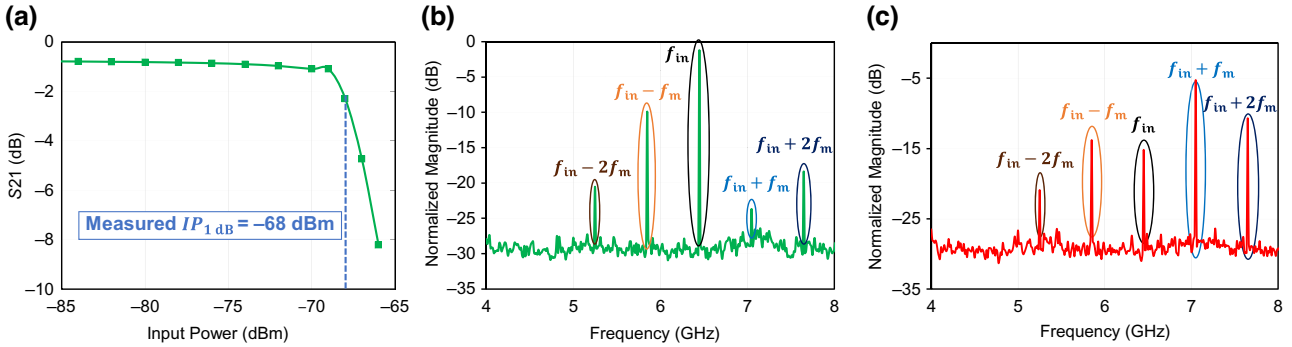

FIG. 6. (a) Measured S_{21} at center frequency across varying input power. Measured output spectra normalized to the input power (b) in the forward direction and (c) in the reverse direction.

of magnitude larger than the typical power used to readout and control the superconducting qubits. Normalized output spectra in the forward and reverse directions are depicted in Figs. 6(b) and 6(c), respectively. In the transmission direction most of the input power is concentrated at the input frequency, thus representing low insertion loss. In the reverse direction, however, the input power is translated to intermodulation frequencies resulting in high isolation. Reducing the signal power translation to IM frequencies and consequently reducing the harmonic losses through differential architecture similar to the differential circulators discussed in Sec. III and similar to Ref. [31] would be an interesting research direction.

V. CHALLENGES AND FUTURE OUTLOOK

While time-modulated superconducting nonreciprocal components offer several advantages over their ferrite counterparts such as easier system integration, low cost, small size, and easier scalability to large systems, they are not without limitations. One challenge in the current implementation is the generation of multiple modulation signals that go between the cryogenic and room-temperature stages. This issue can be easily circumvented by implementing on-chip phase-generation circuitry by leveraging passive superconducting hybrid couplers [41] and tunable phase shifters [42], thus

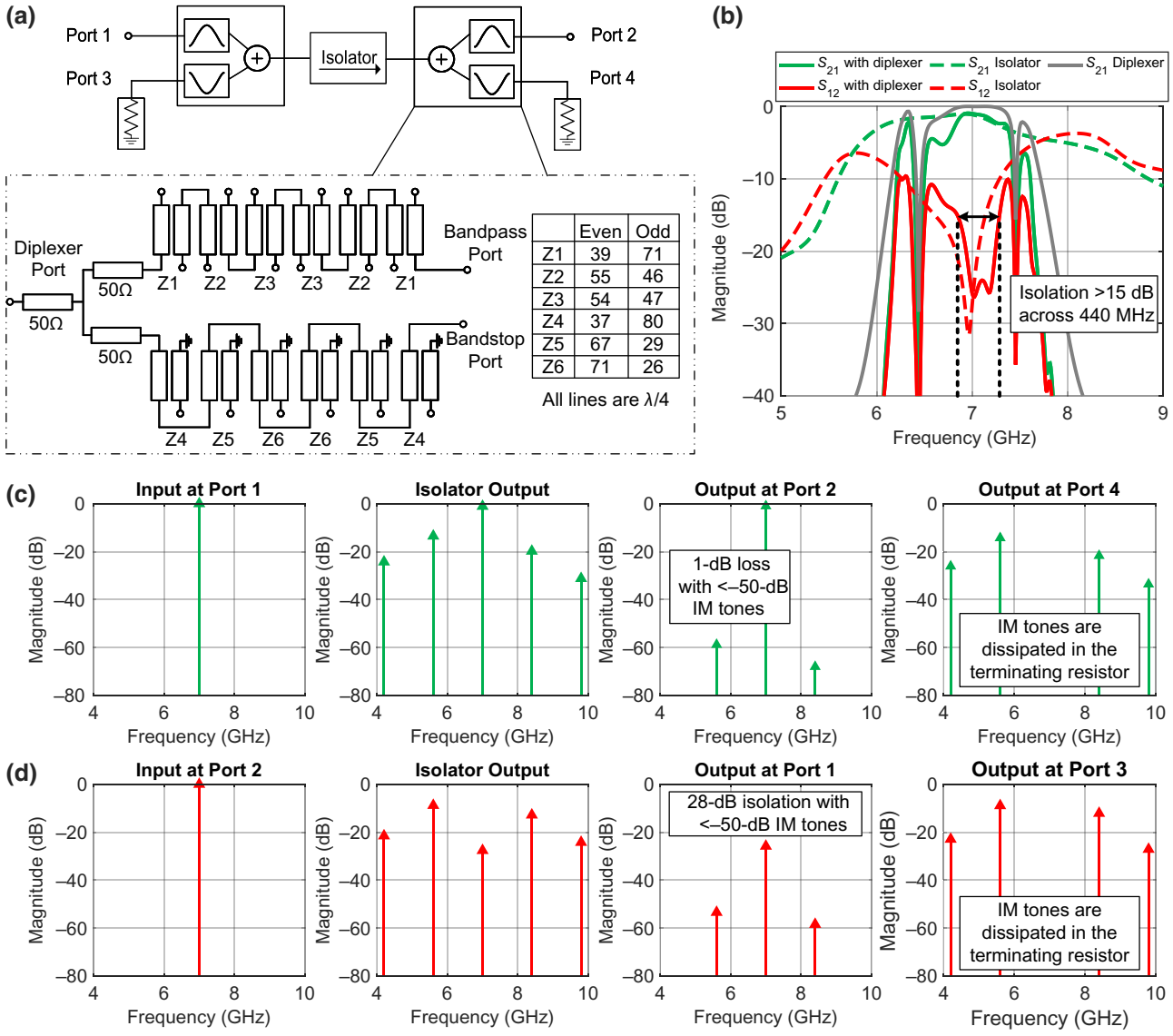

FIG. 7. (a) Block diagram with frequency diplexers to separate the in-band signals and out-of-band IM products generated by the isolator, and diplexer schematic with even and odd impedance values. (b) Simulated small-signal performance of coupled-resonator-based isolator with fifth-order *LC*-based bandpass and bandstop diplexers. (c) Incident signal at port 1, and output signals at the output of isolator, port 2 and port 4, showcasing low transmission loss with >50-dB IM suppression. (d) Incident signal at port 2, and output signals at the output of isolator, port 1 and port 3, showcasing high isolation with >50-dB IM suppression.

reducing the number of coaxial cables and their associated heat loading.

In addition, the time-modulated superconducting isolator generates isolation by translating the in-band power to out-of-band IM frequencies at an offset of $\pm kf_{\mathrm{m}}$ where $k = 1, 2, 3, \ldots$ In a single-qubit system, this frequency is much greater than any relevant bandwidth and can be considered to be far-off resonant [43]. However, in multiqubit systems, these IM tones may interfere with neighboring qubits. To circumvent this limitation, we propose to separate the spurious tones at the IM frequencies from the input-output signals by sandwiching the isolator between two frequency diplexers as depicted in Fig. 7(a). Essentially, the in-band tones with no frequency translation are transmitted to the input-output ports through the bandpass port of the diplexer, while the frequency-translated IM tones generated by the isolator are filtered through the bandstop port of the diplexer and dissipated in the termination ports 3 and 4. For a successful implementation, the diplexer in-band bandwidth should be larger than the nonreciprocal bandwidth of the time-modulated isolator and should be smaller than the modulation frequency, f_m, for effective filtering of the IM tones. To illustrate this concept, we designed a fifth-order bandpass and bandstop diplexers with an in-band bandwidth of 700 MHz using coupled microstrips. Each diplexer has a total of ten quarter wavelength coupled transmission lines and three single-ended quarter-wavelength transmission lines. The even and odd impedances of the coupled transmission lines are listed in Fig. 7(a). Each transmission line occupies an area $<0.2 \times 2.2$ mm^2 with $2\times$ meandering, thus leading to a total area of approximately equal to 2 mm $\times$ 2.2 mm $= 4.4$ mm^2 per frequency diplexer. Therefore, we estimate that the total area of the diplexer-isolator-diplexer will be approximately equal to 12 mm^2. The frequency diplexer is EM simulated in Keysight ADS and exhibits <0.1-dB insertion loss in the passband and this insertion loss is comparable with prior superconducting bandpass filters [44,45].

The frequency diplexer is combined with the time-modulated isolator for s parameters to obtain input-output spectra as depicted in Figs. 7(b)–7(d). Here the isolator is modulated at 1.4 GHz achieving an isolation bandwidth of approximately equal to 500 MHz [dashed lines in Fig. 7(b)], and the bandpass bandwidth of the diplexer is 700 MHz [gray line in Fig. 7(b)]. The combined diplexer-isolator-diplexer structure achieves an insertion loss <1.3 dB with isolation greater than >15 dB across a bandwidth of 440 MHz. The isolation bandwidth is limited by the bandwidth of the isolator and the out-of-band filtering is primarily achieved by the frequency diplexer. The transmission and isolation spectra of the structure are depicted in Figs. 7(c) and 7(d). In the forward direction, for a 7-GHz signal incident at port 1, the isolator output generated IM tones along with the in-band tone. Upon the filtering from the frequency diplexer, all the IM tones are dissipated in a terminating resistor (port 4) and only the in-band tone passes to the output port (port 2), achieving an IM rejection >50 dB at the output port. Thus achieving a low-loss transmission with <-50-dB IM conversion. Similarly, when a 7-GHz tone is incident at port 2, the isolator achieves >20-dB isolation at input frequency (7 GHz) albeit with high IM tones (approximately equal to -5 dB). These large IM tones are filtered by the frequency diplexer and are dissipated in a terminating resistor (port 3). Only the small residue in-band signal propagates to port 1, thus resulting in a high isolation (>20 dB) with very small IM conversion (<-50 dB) that is limited by the filtering profile of the diplexer. It has to be noted that these frequency diplexers can be readily integrated with the isolator and can be included in the superconducting fabrication process. The diplexers can be implemented either as an LC equivalent or transmission line equivalent and such integrated frequency diplexers are commonly used in present-day wireless radios [36]. Integration of the frequency diplexers along with the time-modulated isolator will be a part of future work.

VI. CONCLUSION

This paper presented the concept of time-modulated coupled resonator networks as a means to develop on-chip, magnetless nonreciprocal components for quantum computing systems. We demonstrated that conventional SQUID-based resonators can serve as unit elements and can be combined in series to realize an on-chip nonreciprocal responses. These coupled-resonator networks provide reconfigurable reciprocal and nonreciprocal responses that are solely dependent on the modulation parameters, such as the static flux bias, modulation amplitude, frequency, and phase staggering. We discussed the design procedure of these nonreciprocal components and evaluated their performance using spectral-$ABCD$ matrices. Later, we validated our theoretical findings by implementing and measuring an isolator based on three series-coupled resonator networks, thus demonstrating the potential of such networks for future quantum computing systems. Finally, we discussed the current limitations of coupled-resonator-based isolators, such as the multiphase pump requirement and IM tone generation, as well as potential methodologies for addressing these limitations. By integrating devices in this manner, existing control and readout chains can be simplified, and alternative control and readout methods can be enabled that are not feasible with commercially available nonreciprocal components.

ACKNOWLEDGMENTS

This work is supported by McKelvey Collaboration Initiation Grant (CIG) 2022, and by NSF Grant No. PHY-1752844 (CAREER), and the Air Force Office of Scientific Research (AFOSR) Multidisciplinary University Research

Initiative (MURI) Award on Programmable systems with non-Hermitian quantum dynamics (Grant No. FA9550-21-1- 0202) and use of facilities at the Institute of Materials Science and Engineering at Washington University.

APPENDIX: SPECTRAL-ADMITTANCE MATRIX OF A TIME-VARYING INDUCTOR

The voltage and current relationship of a time-varying inductor [34,35] can be expressed as

$$i(t) = L(t)^{-1} \int v(t)dt. \tag{A1}$$

When the inductance is modulated with a fundamental frequency of ω_m and input excitation is at ω, the voltage and current would carry the IM products and can be expressed as

$$i(t) = \sum_{p=-k}^{k} I(\omega + p\omega_m) e^{-j(\omega+p\omega_m)t}, \tag{A2}$$

$$v(t) = \sum_{p=-k}^{k} V(\omega + p\omega_m) e^{-j(\omega+p\omega_m)t}, \tag{A3}$$

where $I(\omega + p\omega_m)$ and $V(\omega + p\omega_m)$ are the current and voltage Fourier coefficients of the frequency $(\omega + p\omega_m)$, and k is the farthest IM product that has been calculated. The value of k determines the accuracy of the computation and as $k \to \infty$ the computation error $\to 0$. This current and voltage can be expressed in matrix form as

$$\underline{I} = \begin{bmatrix} \vdots \\ I(\omega - 2\omega_m) \\ I(\omega - \omega_m) \\ I(\omega) \\ I(\omega + \omega_m) \\ I(\omega + 2\omega_m) \\ \vdots \end{bmatrix}, \tag{A4}$$

$$\underline{V} = \begin{bmatrix} \vdots \\ V(\omega - 2\omega_m) \\ V(\omega - \omega_m) \\ V(\omega) \\ V(\omega + \omega_m) \\ V(\omega + 2\omega_m) \\ \vdots \end{bmatrix}. \tag{A5}$$

Therefore, the integral of voltage can be calculated as

$$\int \underline{V(t)}dt = \begin{bmatrix} \frac{V(\omega - k\omega_m)}{j(\omega - k\omega_m)} \\ \vdots \\ \frac{V(\omega)}{j\omega} \\ \vdots \\ \frac{V(\omega + k\omega_m)}{j(\omega + k\omega_m)} \end{bmatrix} = \underline{\Omega} \times \underline{V}, \tag{A6}$$

where

$$\underline{\Omega} = \begin{bmatrix} \frac{1}{j(\omega - k\omega_m)} & 0 & 0 & 0 & 0 \\ 0 & \ddots & \vdots & \iddots & 0 \\ 0 & \cdots & \frac{1}{j(\omega)} & \cdots & 0 \\ 0 & \iddots & \vdots & \ddots & 0 \\ 0 & 0 & 0 & 0 & \frac{1}{j(\omega + k\omega_m)} \end{bmatrix}. \tag{A7}$$

Therefore, Eq. (A1) can be expressed in spectral matrix form as

$$\underline{I} = \mathcal{F}(L(t)^{-1}) * (\underline{\Omega} \times \underline{V}) = \underline{Y_L} \times \underline{V}. \tag{A8}$$

[1] F. Arute, *et al.*, Quantum supremacy using a programmable superconducting processor, Nature **574**, 505 (2019).

[2] J. C. Bardin, D. Sank, O. Naaman, and E. Jeffrey, Quantum computing: An introduction for microwave engineers, IEEE Microw. Mag. **21**, 24 (2020).

[3] J. C. Bardin, D. H. Slichter, and D. J. Reilly, Microwaves in quantum computing, IEEE J. Microw. **1**, 403 (2021).

[4] B. D. Josephson, Possible new effects in superconductive tunneling, Phys. Lett. **1**, 251 (1962).

[5] P. W. Anderson and J. M. Rowel, Probable observation of the Josephson superconducting tunneling effect, Phys. Rev. Lett. **10**, 230 (1963).

[6] L. Ranzani and J. Aumentado, Circulators at the quantum limit: Recent realizations of quantum-limited superconducting circulators and related approaches, IEEE Microw. Mag. **20**, 112 (2019).

[7] A. Nagulu, N. Reiskarimian, and H. Krishnaswamy, Nonreciprocal electronics based on temporal modulation, Nat. Electron. **3**, 241 (2020).

[8] A. Kord, D. L. Sounas, and A. Alù, Microwave nonreciprocity, Proc. IEEE **108**, 1728 (2020).

[9] R. Fleury, *et al.*, Sound isolation and giant linear nonreciprocity in a compact acoustic circulator, Science **343**, 516 (2014).

[10] M. M. Torunbalci, T. J. Odelberg, S. Sridaran, R. C. Ruby, and S. A. Bhave, An FBAR circulator, IEEE Microw. Wirel. Compon. Lett. **28**, 395 (2018).

[11] Y. Yu, G. Michetti, A. Kord, D. Sounas, F. V. Pop, P. Kulik, M. Pirro, Z. Qian, A. Alu, and M. Rinaldi, in *2018 IEEE Micro Electro Mechanical Systems (MEMS)* (IEEE, Belfast, UK, 2018), p. 154, https://ieeexplore.ieee.org/document/8346507.
[12] A. Kamal, A parametric device as a nonreciprocal element, Proc. IRE **48**, 1424 (1960).
[13] N. A. Estep, D. L. Sounas, J. Soric, and A. Alù, Magnetic-free non-reciprocity and isolation based on parametrically modulated coupled-resonator loops, Nat. Phys. **10**, 923 (2014).
[14] N. Reiskarimian and H. Krishnaswamy, Magnetic-free non-reciprocity based on staggered commutation, Nat. Commun. **7**, 11217 (2016).
[15] T. Dinc, M. Tymchenko, A. Nagulu, D. Sounas, A. Alù, and H. Krishnaswamy, Synchronized conductivity modulation to realize broadband lossless magnetic-free non-reciprocity, Nat. Commun. **8**, 795 (2017).
[16] M. M. Biedka, R. Zhu, Q. M. Xu, and Y. E. Wang, Ultra-wide band non-reciprocity through sequentially-switched delay lines, Sci. Rep. **7**, 40014 (2017).
[17] T. T. Koutserimpas and C. Valagiannopoulos, Multiharmonic resonances of coupled time-modulated resistive metasurfaces, Phys. Rev. Appl. **19**, 064072 (2023).
[18] F. D. M. Haldane and S. Raghu, Possible realization of directional optical waveguides in photonic crystals with broken time-reversal symmetry, Phys. Rev. Lett. **100**, 013904 (2008).
[19] L. D. Tzuang, K. Fang, P. Nussenzveig, S. Fan, and M. Lipson, Non-reciprocal phase shift induced by an effective magnetic flux for light, Nat. Photonics **8**, 701 (2014).
[20] N. Chamanara, S. Taravati, Z.-L. Deck-Léger, and C. Caloz, Optical isolation based on space-time engineered asymmetric photonic band gaps, Phys. Rev. B **96**, 155409 (2017).
[21] J. Kerckhoff, K. Lalumière, B. J. Chapman, A. Blais, and K. W. Lehnert, On-chip superconducting microwave circulator from synthetic rotation, Phys. Rev. Appl. **4**, 034002 (2015).
[22] B. J. Chapman, *et al.*, Widely tunable on-chip microwave circulator for superconducting quantum circuits, Phys. Rev. X **7**, 041043 (2017).
[23] F. Lecocq, *et al.*, Nonreciprocal microwave signal processing with a field-programmable Josephson amplifier, Phys. Rev. Appl. **7**, 024028 (2017).
[24] B. Abdo, M. Brink, and J. M. Chow, Gyrator operation using Josephson mixers, Phys. Rev. Appl. **8**, 034009 (2017).
[25] L. Ranzani, S. Kotler, A. J. Sirois, M. P. DeFeo, M. Castellanos-Beltran, K. Cicak, L. R. Vale, and J. Aumentado, Wideband isolation by frequency conversion in a Josephson-junction transmission line, Phys. Rev. Appl. **8**, 054035 (2017).
[26] C. Müller, S. Guan, N. Vogt, J. H. Cole, and T. M. Stace, Passive on-chip superconducting circulator using a ring of tunnel junctions, Phys. Rev. Lett. **120**, 213602 (2018).
[27] B. J. Chapman, E. I. Rosenthal, and K. W. Lehnert, Design of an on-chip superconducting microwave circulator with octave bandwidth, Phys. Rev. Appl. **11**, 044048 (2019).
[28] V. Fatemi, A. R. Akhmerov, and L. Bretheau, Weyl Josephson circuits, Phys. Rev. Res. **3**, 013288 (2021).
[29] B. Richman and J. M. Taylor, Circulation by microwave-induced vortex transport for signal isolation, PRX Quantum **2**, 030309 (2021).
[30] M. A. Beck, M. Selvanayagam, A. Carniol, S. Cairns, and C. P. Mancini, Wideband Josephson parametric isolator, Phys. Rev. Appl. **20**, 034054 (2023).
[31] A. Kord, D. L. Sounas, and A. Alù, in *2017 IEEE MTT-S International Microwave Symposium (IMS)* (IEEE, Honolulu, HI, USA, 2017), p. 384, https://ieeexplore.ieee.org/document/8058574.
[32] X. Wu, *et al.*, Isolating bandpass filters using time-modulated resonators, IEEE Trans. Microw. Theory Tech. **67**, 2331 (2019).
[33] A. Alvarez-Melcon, X. Wu, J. Zang, X. Liu, and J. S. Gomez-Diaz, Coupling matrix representation of nonreciprocal filters based on time-modulated resonators, IEEE Trans. Microw. Theory Tech. **67**, 4751 (2019).
[34] C. Desoer, Steady-state transmission through a network containing a single time-varying element, IRE Trans. Circuit Theory **6**, 244 (1959).
[35] C. Kurth, Steady-state analysis of sinusoidal time-variant networks applied to equivalent circuits for transmission networks, IEEE Trans. Circuits Syst. **24**, 610 (1977).
[36] D. M. Pozar, *Microwave Engineering* (Wiley, 1998), https://books.google.com/books/about/Microwave_Engineering.html?id=0XLFQgAACAAJ&source=kp_book_description.
[37] R. Fleury, A. B. Khanikaev, and A. Alu, Floquet topological insulators for sound, Nat. Commun. **7**, 11744 (2016).
[38] A. Kord, D. L. Sounas, and A. Alù, Magnet-less circulators based on spatiotemporal modulation of bandstop filters in a delta topology, IEEE Trans. Microw. Theory Tech. **66**, 911 (2018).
[39] O. Naaman and J. Aumentado, Synthesis of parametrically coupled networks, PRX Quantum **3**, 020201 (2022).
[40] L. Ranzani, L. Spietz, Z. Popovic, and J. Aumentado, Two-port microwave calibration at millikelvin temperatures, Rev. Sci. Instrum. **84**, 034704 (2013).
[41] N. K. Khaira, T. Singh, and R. R. Mansour, in *2022 IEEE/MTT-S International Microwave Symposium—IMS 2022* (IEEE, Denver, CO, USA, 2022), p. 160, https://ieeexplore.ieee.org/document/9865430.
[42] T. Singh, N. K. Khaira, and R. R. Mansour, Thermally actuated SOI RF MEMS-based fully integrated passive reflective-type analog phase shifter for mmWave applications, IEEE Trans. Microw. Theory Tech. **69**, 119 (2021).
[43] A. Blais, A. L. Grimsmo, S. M. Girvin, and A. Wallraff, Circuit quantum electrodynamics, Rev. Mod. Phys. **93**, 025005 (2021).
[44] N. Sekiya and T. Tsuruoka, Improvement of filter properties of independently tunable superconducting dual-band bandpass filter, IEEE Trans. Appl. Supercond. **29**, 1 (2019).
[45] K. Sakuma, S. Rachi, G. Mizoguchi, T. Nakajima, A. Mizuno, and N. Sekiya, A superconducting dual-band bandpass filter for IF signals of multi-frequency millimeter-wave atmospheric spectrometer, IEEE Trans. Appl. Supercond. **33**, 1 (2023).

Correction: Reference [30] did not contain proper source information and has been fixed.